Research Square

Preprints are preliminary reports that have not undergone peer review.
They should not be considered conclusive, used to inform clinical practice,
or referenced by the media as validated information.

Robust Iron-based Fischer-Tropsch Catalysts by Direct Joule Synthesis

Amol Amrute

amol_amrute@a-star.edu.sg

Institute of Sustainability for Chemicals, Energy and Environment (ISCE2), Agency for Science, Technology and Research (A*STAR) https://orcid.org/0000-0002-3362-0842

Jose Recatala-Gomez

Berkeley Education Alliance for Research in Singapore (BEARS) and University of California, Berkeley, California

Somya Verma

Nanyang Technological University and Institute of Sustainability for Chemicals, Energy and Environment (ISCE2)

Puneethkumar Srinivasappa

Berkeley Education Alliance for Research in Singapore (BEARS) and Institute of Sustainability for Chemicals, Energy and Environment (ISCE2)

Mona Abdelgaid

University of California, Berkeley, California https://orcid.org/0000-0003-0973-3262

Tangsheng Zou

Institute of Sustainability for Chemicals, Energy and Environment (ISCE2), Agency for Science, Technology and Research (A*STAR) https://orcid.org/0000-0001-7989-4489

Seohyeong Lee

Nanyang Technological University

Delwin Tanto

Nanyang Technological University https://orcid.org/0009-0006-7636-1664

Pei Ying Moo

Institute of Sustainability for Chemicals, Energy and Environment (ISCE2), Agency for Science, Technology and Research (A*STAR)

Chun Qi Joy Ng

Institute of Sustainability for Chemicals, Energy and Environment (ISCE2), Agency for Science, Technology and Research (A*STAR)

Chuandayani Gwie

Institute of Sustainability for Chemicals, Energy and Environment (ISCE2), Agency for Science, Technology and Research (A*STAR)

Chenguang Zhang

Nanyang Technological University https://orcid.org/0000-0003-4658-5633

Zainul Aabdin

e Institute of Materials Research and Engineering (IMRE), Agency for Science, Technology and Research (A*STAR)

Kristin Persson

University of California, Berkeley, and Lawrence Berkeley National Laboratory Berkeley https://orcid.org/0000-0003-2495-5509

Kedar Hippalgaonkar

Nanyang Technological University https://orcid.org/0000-0002-1270-9047

Article

Keywords:

Posted Date: November 6th, 2026

DOI: https://doi.org/10.21203/rs.3.rs-11385922/v1

License: This work is licensed under a Creative Commons Attribution 4.0 International License. Read Full License

Additional Declarations: There is **NO** Competing Interest.

Robust Iron-based Fischer-Tropsch Catalysts by Direct Joule Synthesis

Jose Recatala-Gomez,‡[a,b] Somya Verma,‡[a,c,d] Puneethkumar M. Srinivasappa,[a,c] Mona Abdelgaid,[b,f,g] Tangsheng Zou,[c] Seohyeong Lee,[d] Delwin Tanto,[d] Pei Ying Moo,[c] Chun Qi Joy Ng,[c] Chuandayani Gunawan Gwie,[c] Chenguang Zhang,[d] Zainul Aabdin,[e] Kristin A. Persson,[b,f,g] Kedar Hippalgaonkar,[a,d] Amol Amrute*[c]*

[a] Berkeley Education Alliance for Research in Singapore (BEARS), 1 Create Way, #05-02/03, CREATE Tower, 138602 Singapore

[b] Department of Materials Science & Engineering, University of California, Berkeley, California 94720, United States

[c] Institute of Sustainability for Chemicals, Energy and Environment (ISCE^2), Agency for Science, Technology and Research (A*STAR), 1 Pesek Road, Jurong Island, 627833, Singapore

[d] School of Materials Science and Engineering, Nanyang Technological University, 50 Nanyang Avenue, 639798 Singapore

[e] Institute of Materials Research and Engineering (IMRE), Agency for Science, Technology and Research (A*STAR), 2 Fusionopolis Way, #08-03 Innovis, Singapore 138634

[f] Bakar Institute of Digital Materials for the Planet, University of California at Berkeley, Berkeley, California 94720, United States

[g] Materials Science Division, Lawrence Berkeley National Laboratory, Berkeley, California 94720, United States

*Correspondence authors: ***kedar@ntu.edu.sg***, ***amol_amrute@a-star.edu.sg***

Abstract: Converting CO_2 into gasoline- and jet-fuel-range hydrocarbons offers an elegant approach to sustainable fuels compatible with existing infrastructure. However, widely applied iron-based syngas Fischer-Tropsch catalysts deactivate in CO_2-rich feeds due to oxidation of active carbides in oxidising CO_2 environments and the doubled H_2O byproduct. Herein, we demonstrate Direct Joule Synthesis (DJS) coupled with mechanochemical treatment as an effective method to prepare metal-rich Fe-Co-Na precursors, which reconstruct during CO_2 hydrogenation into carbide-containing active structures. The optimised FeCoNa sample attains 57.3% CO_2 conversion, 24.1% C_{5+} yield, 43.7% C_{2+} yield, and space-time-yields of 0.40 $g_{C_{5+}}\,h^{-1}\,g_{cat}^{-1}$ and 0.68 $g_{C_{2+}}\,h^{-1}\,g_{cat}^{-1}$ at 350°C and 30 bar, exceeding reported systems. Even more intriguing, the stable operation for at least 500 h on stream is achieved due to retention of Fe_5C_2 as a dominant phase, stabilised by residual metallic FeCo acting as a reduction promoter limiting carbide re-oxidation, in addition to enhancing olefin release and supply of adsorbed intermediates. These findings demonstrate the activity and stability advantages of metal-derived Fe-based CO_2 hydrogenation catalysts, establishing DJS as a rapid non-equilibrium synthesis method for versatile multimetallic catalysts.

MAIN

The rising atmospheric carbon dioxide (CO_2) concentration exceeding pre-industrial levels presents a critical challenge to climate stability, necessitating solutions to reduce emissions in the chemical and energy sectors.[1] Power-to-liquid fuels or chemicals offer a scalable decarbonisation opportunity by using green H_2 and captured CO_2 to (1) produce high-energy-density fuels that are compatible with existing infrastructure and (2) produce platform chemicals such as olefins, methanol, and naphthalene. To this end, thermocatalytic CO_2 hydrogenation has emerged as a

promising pathway towards carbon-neutral gasoline and jet fuel-range hydrocarbons.[2,3] Modified Fischer-Tropsch (FT) synthesis using multifunctional catalysts offers a direct route for this transformation.[4,5]

Fe and Co serve as widely used industrial catalyst metals for FT synthesis,[6] with FT plants accounting for the majority of the Fe-based catalysts utilised industrially. Direct CO_2 hydrogenation to longer-chain hydrocarbons, however, is not yet an established commercial technology because high conversion, chain-growth selectivity, and long-term stability remain difficult to achieve simultaneously.[7] Fe catalysts are also attractive for this chemistry because Fe_3O_4 facilitates the reverse water-gas shift (rWGS) reaction, whereas iron carbides, particularly χ-Fe_5C_2, promote C-C coupling and hydrocarbon chain growth.[7,8] Maintaining these carbide phases is more challenging in CO_2-based feedstocks because of the greater oxidising nature of CO_2, inducing the transformation of χ-Fe_5C_2 into Fe_3O_4 with an accompanying loss of activity.[9] Furthermore, as twice as many H_2O molecules are generated compared to syngas-based FT, the resulting increase in water partial pressure further inhibits catalyst performance, which depends on continuous competition between carburisation and H_2O-induced oxidation.[10,11] Although promoters can facilitate carburisation of Fe-based catalysts, maintaining the resulting carbide phases against re-oxidation during CO_2 hydrogenation remains challenging.[12]

Despite this compositional tuning, simultaneously achieving high hydrocarbon productivity with long-term stability is still hampered by the intrinsic difficulty in controlling the dynamic competition between reduced, carbidic, and oxidic Fe states arising from *in situ* phase evolution between phases. Long-duration stability assessments under high-conversion conditions remain particularly scarce.

Traditionally, Fe-based catalysts are synthesised *via* solution methods such as coprecipitation and hydrothermal routes, resulting primarily in oxide-based pre-catalysts, which convert into mixed oxide-carbide systems under CO_2 hydrogenation conditions, typically after reduction (in H_2) and activation (in $CO+H_2$) prior to reaction. However, oxide-derived iron carbides remain susceptible to re-oxidation during CO_2 hydrogenation, with reaction-generated water promoting their transformation into Fe_3O_4.[11] The susceptibility of re-oxidation of oxide-derived carbides leads to the hypothesis that a primarily metallic Fe-containing phase could be a more effective alternative precursor state for controlling phase evolution and sustaining a productive carbide-containing working state during prolonged CO_2 hydrogenation.

Addressing this design question requires different synthesis strategies that produce a variety of phases and alternative morphologies. Dry, solvent-free methods, such as mechanochemical processing, combustion synthesis, and ultrafast thermal treatments, enable access to non-equilibrium structures and metastable phases that are difficult to achieve through conventional wet routes.[3,13,14] Mechanochemical approaches promote intimate mixing of metals and promoters while generating defect-rich, highly dispersed structures.[13] Joule-heating-based synthesis also helps suppress oxidation and preserve distinct nano- and microstructures, including metallic and/or alloyed phases.[15,16] Exploiting these synthesis methods in a metal-first approach provides a fundamentally different starting point from conventional oxide-rich precursors, enabling investigation of how an initial metallic state influences subsequent carburisation and resistance to reaction-induced re-oxidation, thereby influencing long-term catalytic stability. To our knowledge, Joule-heating synthesis of a thermocatalyst has not yet been reported for the preparation of Fe-based catalysts for CO_2 hydrogenation for fuel production.

In this work, we combine Direct Joule synthesis (DJS) followed by high-energy milling to obtain FeCoNa materials that are highly active in CO_2 hydrogenation towards C_{2+} products and gasoline- and jet-fuel-range hydrocarbons (C_{5+}) with unprecedented stability. Despite its initially low surface area and large crystallite size, the pre-catalyst rich in metallic Fe-containing phases transforms into smaller, defect-rich carbide- and oxide-containing structures under CO_2 hydrogenation conditions while maintaining small amount of FeCo that acts as reduction promoter. The optimised Ar-milled catalyst achieves 57.3% CO_2 conversion, 76.3% total C_{2+} product selectivity, 42.1% C_{5+} selectivity, corresponding to C_{2+} yield of 43.7% at 350 °C and 30 bar. Increasing the space velocity approximately doubles C_{5+} productivity while retaining nearly the same single-pass yield, and a separate 500 h test demonstrates sustained conversion and C_{5+} selectivity. These results establish a metal-first catalyst-design strategy that couples rapid precursor synthesis with the formation and retention of a productive multiphase catalyst. DFT calculations further suggest that Na-promoted χ-Fe_5C_2 favours carbon-chain growth, while residual FeCo supports hydrogen adsorption and exhibits a weak driving force for re-oxidation, consistent with its role as an intrinsic reduction promoter.

RESULTS

Direct Joule synthesis approach of Fe-based FTS catalyst precursors

Direct Joule synthesis (DJS, **Fig. 1a**) was employed to prepare metallic FeCo-rich pre-catalysts.[17] Compared with conventional wet-chemical routes such as co-precipitation, impregnation, and sol-gel synthesis, which typically involve multi-step solution processing and often yield oxide-dominated products,[18,19] DJS enables the formation of alloy phases under highly localised Joule heating conditions. **Fig. 1b** shows a typical temperature *versus* time profile measured for DJS

synthesis of $Fe_{85}Co_{10}Na_5$. Although the synthesis is conducted in air, the thermal decomposition of the carbon felt creates a reducing atmosphere, promoting *in situ* reduction and alloy formation.

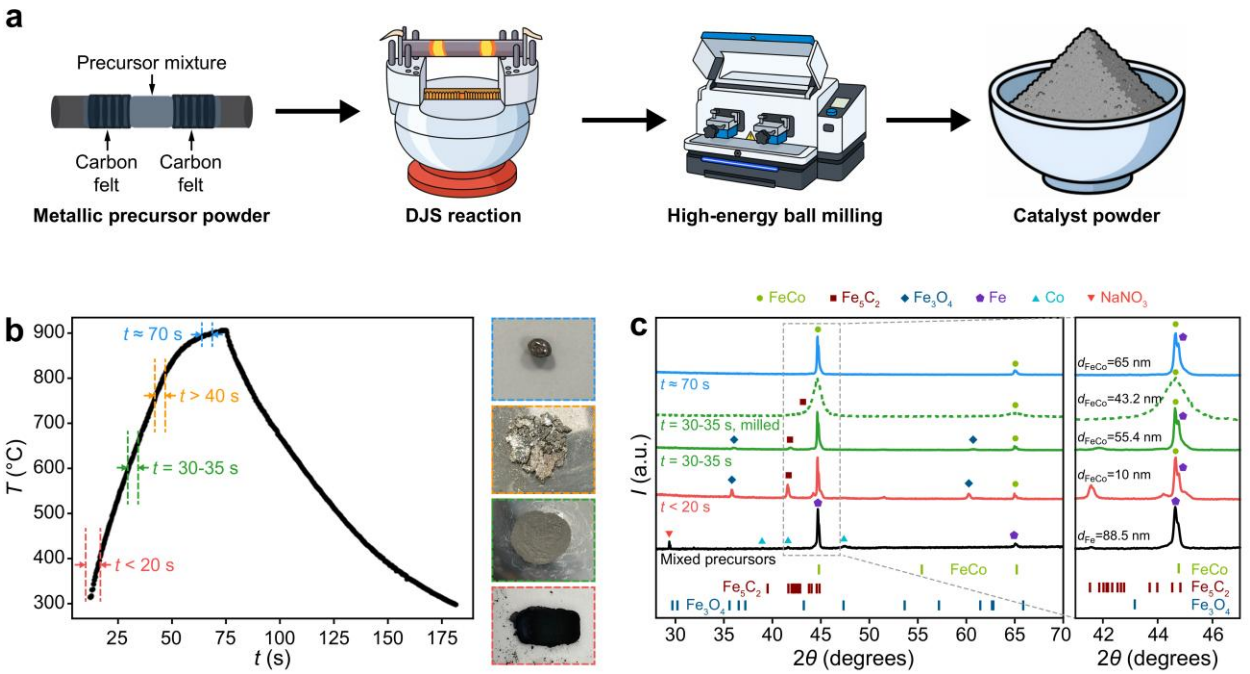


Fig. 1. **Direct Joule synthesis and phase evolution of FeCoNa catalysts.** (a) Schematic illustration of solvent-free Fe-based catalyst synthesis *via* a combined DJS and ball milling approach. (b) Typical temperature *versus* time profile measured during a DJS process. Pictures of samples collected at various time intervals, shown on the profile with coloured vertical lines, are presented on the right panel. (c) X-ray diffraction patterns of FeCoNa samples collected after different time intervals.

To investigate the evolution of crystalline phases formed during DJS, the current was stopped at different time intervals, and the resultant materials were characterised by X-ray diffraction (XRD). Regardless of heating duration, a prominent diffraction peak at 2θ ~45° was indexed to the FeCo alloy (ICSD #56273) and was observed in all samples (**Fig. 1c**), confirming it as the dominant crystalline phase. At short durations (<20 s), a black to dark-grey product was obtained, suggesting

the initial formation of a metallic alloy phase (as highlighted in **Fig. 1b**, dashed red region). Additional diffraction peaks corresponding to Fe_3O_4 (ICSD #162349) were observed, in line with partial oxidation, as the synthesis was carried out in air. At intermediate durations (~30-35 s), a gradual transition from dark grey to light grey was observed, along with a sharpening of the peak at 2θ ~45° (**Fig. 1c**), suggesting progressive alloy formation and crystallite growth. Notably, a broad peak at 2θ ~42.3° was indexed to Fe_5C_2 (ICSD #245334), consistent with the reducing nature of DJS, as the burning of carbon felt at high temperatures releases CO, which prevents excessive oxidation and induces carburisation of the metallic alloy. Pronounced powder sintering occurred for synthesis durations above 40 s, characterised by large FeCo crystals (**Fig. 1c**). Durations beyond 70 s led to the formation of a dense, pellet-like material due to extensive sintering. Materials synthesised at an intermediate reaction time (~30-35 s) produced metal-rich powders with an average FeCo crystallite size of 55.4 nm (**Table S1**). Scanning electron microscopy (SEM) revealed micron-scale particles with irregular shapes, while energy-dispersive X-ray (EDS) spectroscopy mapping showed spatial variations in elemental composition (**Fig. S1**). As the FeCoNa material as synthesised possessed a relatively small specific surface area of 1.2 $m^2\ g^{-1}$ **(Table S1)**, it was subsequently subjected to high-energy ball milling to reduce the crystallite size and further promote the formation of an oxide-depleted, alloy-rich starting state, as discussed in the following section.

Post-synthetic modification of DJS-derived catalysts by ball milling

As a baseline, the catalytic performance of DJS as-derived FeCoNa material i.e. without any post-synthesis processing or treatment in CO_2 hydrogenation was evaluated at 350 °C, 30 bar, and a gas hourly space velocity (GHSV) of 5732 $cm^3\ h^{-1}\ g_{cat}^{-1}$ achieving a CO_2 conversion of 35.7%, with

a poor C_{2+} selectivity of 43.6%, C_{5+} selectivity of 15.7% and a corresponding C_{5+} yield of 5.6%. In addition, a relatively high CH_4 selectivity of 28.9% was observed, indicating substantial methanation activity under reaction conditions. The limited selectivity towards long-chain hydrocarbons, together with the pronounced CH_4 formation, likely stems from the low density of suitable active sites arising from the sintered nature of the as-synthesised DJS materials. To address this issue, the as-synthesised DJS samples were subjected to high-energy milling, which aims to decrease the particle size and increase active site density to boost catalytic activity. We performed a systematic study to investigate the effect of milling parameters on structural evolution. The as-synthesised DJS sample (FeCoNa) was ball milled at 25 Hz for durations of 2, 4, and 8 h in air. To further examine the influence of milling frequency, experiments at 30 Hz and 4 h (FeCoNa-B30-4) were also conducted. Subsequently, milling was also performed under an inert atmosphere (Ar) to probe the role of atmospheric conditions (FeCoNa-B25-4-Ar).

From the XRD patterns of catalysts after ball milling (**Fig. 2a**), broadening of the FeCo(110) peak at 2θ ~45° was observed for all samples relative to the as-synthesised FeCoNa samples, indicating a reduction in crystallite size. Greater peak broadening was observed for the samples with an increase in milling time from 2 h to 4 h at the same frequency, but no significant change was observed for all other samples milled at higher frequency and/or longer time than 4 h (**Fig. 2a**). This signals that a steady state is reached during high-energy milling, where fracture-driven size reduction is counterbalanced by cold welding and agglomeration, and has been observed previously in Fe-Co systems.[20] The Fe_3O_4 weight fraction as determined by Rietveld refinement decreased in FeCoNa-B25-2 compared to FeCoNa, with the phase no longer detected after 4 h of milling at all frequencies studied (**Fig. 2a**), attributed to the amorphisation and/or reduction of Fe_3O_4 during high-energy milling.[20,21] This phenomenon was similarly observed in Joule heating-

synthesised $Li_{1.2}Mn_{0.4}Ti_{0.4}O_2$ prepared by similar methods, where the disappearance of XRD peaks corresponding to reduced manganese oxide impurities following high-energy milling was attributed to the impurity being only present at the surface level and being removed, or low crystallinity rendering it undetectable by XRD after milling.[22]

Despite ball milling, all DJS-derived catalysts display very limited N_2-adsorption capacities and low Brunauer-Emmett-Teller (BET) surface areas (**Table S1**), consistent with the formation of large aggregates during DJS. The dense, low-porosity character of these samples reflects the nature of the DJS synthesis, in which spring loading of the material prevents the formation of a porous microstructure.

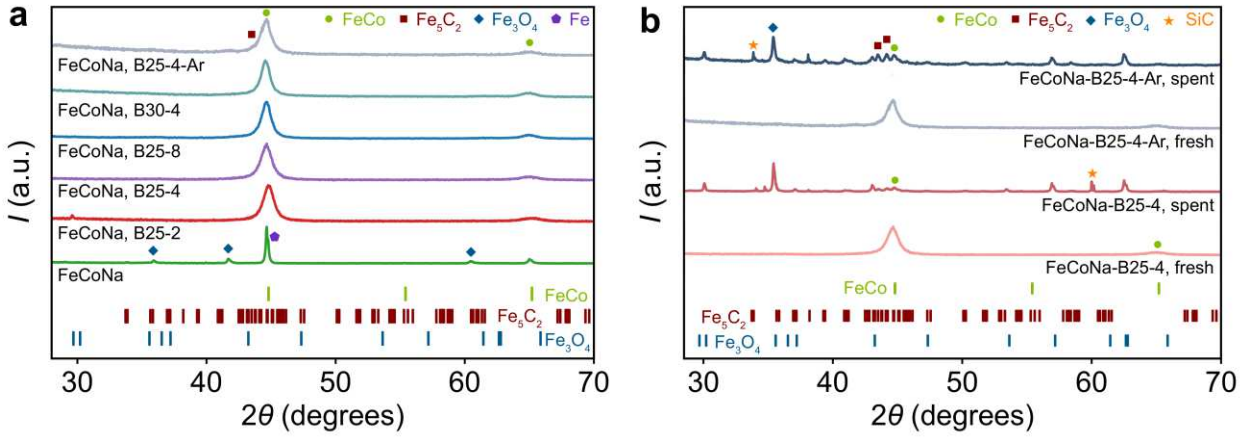


Fig. 2. Powder XRD patterns of DJS-prepared FeCoNa catalysts before and after CO_2 hydrogenation. (a) Powder XRD patterns of DJS-synthesised catalysts subjected to high-energy ball milling under different milling conditions. (b) Diffractograms of FeCoNa catalysts before (fresh) and after (spent) CO_2 hydrogenation reaction.

Table 1. Comparison of catalytic performance, stability, and space time yield of representative Fe-based catalysts for CO_2 hydrogenation.

Entry	Catalyst	*T* (°C)	*P* (bar)	*GHSV* ($cm^3\ h^{-1}\ g_{cat}^{-1}$)	*X*(CO_2) (%)	*S*(C_{2+}) (%)	*S*(C_{5+}) (%)	*Y*(C_{2+}) (%)	*Y*(C_{5+}) (%)	*STY*(C_{2+}) ($g_{C_{2+}}\ h^{-1}\ g_{cat}^{-1}$)	*STY*(C_{5+}) ($g_{C_{5+}}\ h^{-1}\ g_{cat}^{-1}$)	Stability (h)	Ref.
1	FeNa-B25-4	350	30	5732	52.2	76.7	39.3	39.9	20.5	0.33	0.17	>70	This work
2	FeCoNa-B25-4	350	30	5732	57.6	75.9	34.5	43.7	19.9	0.36	0.16	>70	This work
3	FeCoNa-B25-4-Ar	350	30	5732	57.3	76.3	42.1	43.7	24.1	0.36	0.2	500	This work
4	FeCoNa-B25-4-Ar	350	30	11464	52.1	78.7	45.6	41.0	23.7	0.68	0.4	>70	This work
5	Fe-Zn-Zr@HZSM-5-Hbeta	340	50	3000	14.9	59.9	16.3	8.9	2.5	0.04	0.01	10	Wang *et al.* [23]
6	In_2O_3/HZSM-5	340	30	9000	13.1	~54.5	~43.2	7.13	5.7	0.09	0.07	150	Gao *et al.* [2]
7	Na-CoCu/TiO_2	250	50	3000	18.4	51.6	29.4	9.5	5.4	0.04	0.02	200	Shi *et al.* [24]
8	$CuFeO_2$	300	10	1800	17.3	66.5	45.3	11.5	7.8	0.03	0.02	100	Choi *et al.* [25]
9	Fe-Cu-K-La/TiO_2	300	11	3600	23.1	54.0	45.0	12.5	10.4	0.06	0.05	18	Boreriboon *et al.* [26]
10	Fe_2O_3-CT600	350	15	1140	40.0	73.0	36.0	29.2	14.4	0.05	0.02	280	Albrecht *et al.* [27]
11	Na-$ZnFe_2O_4$	340	10	1800	34.0	79.7	51.7	27.1	17.6	0.07	0.05	95	Choi *et al.* [28]
12	Fe-Co/K/Al_2O_3 (F-400)	340	20	—	49.0	67.6	24.9	33.1	12.2	—	—	24	Numpilai *et al.* [29]
13	K-Fe/C + K-ZSM-5	320	20	1200	34.5	72.3	56.9	24.9	19.6	0.05	0.04	50	Guo *et al.* [30]
14	Fe-Mn-K	300	10	2400	38.2	84.6	58.4	32.3	22.3	0.11	0.08	~75	Yao *et al.* [3]
15	10Fe4.8K	300	25	560	35.2	83.6	64.8	29.4	22.8	0.02	0.02	—	Jiang *et al.* [31]
16	NaFe + SAPO-11 + ZSM-5	320	30	1245	31.2	79.4	62.9	24.7	19.6	0.04	0.04	50	Noreen *et al.* [32]
17	10Fe0.8K0.53Co	300	25	560	54.6	79.1	47.0	43.2	25.7	0.03	0.02	—	Jiang *et al.* [31]
18	KZFe-5.0Co	320	20	6000	50.2	—	53.1	—	26.7	—	0.23	60	Guo *et al.* [8]
19	FeNa(1.18)	320	30	2000	40.5	84.2 (wt.%)	30.1 (wt.%)	34.1 (wt.%)	12.2	0.1	0.04	100	Wei *et al.* [33]
20	FeNa	320	30	2040	37.2	76.2	—	28.3	—	0.08	—	12	Liang *et al.* [18]
21	Na-Zn-Fe	340	25	15000	39	75.9	34.8	29.6	13.6	0.64	0.29	70	Zhang *et al.* [34]
22	CoFe-0.81Na	240	30	5500	10.2	78.0	69.1	7.9	7.1	0.06	0.06	120	Zhang *et al.* [35]
23	FeCo	320	30	4000	57.8	81.0	24.3	46.8	14.0	0.27	0.08	50	Pan *et al.* [36]

Performance of DJS-derived post-milled FeCoNa catalysts in CO_2 hydrogenation

To elucidate the role of DJS and subsequent mechanochemical treatment, catalysts subjected to different post-milling conditions were evaluated for CO_2 hydrogenation after reduction in hydrogen, followed by activation in syngas, as detailed in Supplementary Section S2.2. Catalytic testing at 350 °C, 30 bar, and a GHSV of 5732 $cm^3\ h^{-1}\ g_{cat}^{-1}$, demonstrated a clear enhancement in performance compared to the DJS-made FeCoNa (i.e., no post-synthesis milling, **Fig. 3a,b**). The influence of this reduction-activation pretreatment on catalytic performance and the accompanying structural evolution is discussed in Supplementary Section S2.2 (**Figs. S2** and **S3)**. The catalyst ball milled for 2 h at 25 Hz, FeCoNa-B25-2, exhibited a CO_2 conversion of 50.2% (**Fig. 3a**), a C_{5+} selectivity of 30.5%, and a reduced CH_4 selectivity of 19.9%. Increasing the milling time to 4 h (FeCoNa-B25-4) further improved the catalytic performance, achieving 57.6% CO_2 conversion and 34.5% C_{5+} selectivity. Further increase of the milling time to 8 h (FeCoNa-B25-8) provided neither an additional enhancement in hydrocarbon selectivity nor significant improvement in CO_2 conversion. In addition, the catalyst ball milled at a higher frequency of 30 Hz for 4 h (FeCoNa-B30-4) did not exhibit significant improvement in catalytic activity compared to milling at 25 Hz (FeCoNa-B25-4, **Table S2**). Beyond the total C_{5+} selectivity, FeCoNa-B25-4 exhibits selectivities of 21.1% to C_5-C_{10} hydrocarbons and 15.8% to C_8-C_{16} hydrocarbons, corresponding to gasoline- and jet-fuel-range fractions, respectively. The corresponding gasoline- and jet-fuel-range product distributions for all DJS-derived catalysts are provided in **Table S3**.

Based on these observations, the 25 Hz-4 h milling condition emerged as the optimal post-synthesis treatment, providing an effective balance between high CO_2 conversion, enhanced C_{5+} selectivity, and suppressed CH_4 formation. Using this optimised condition, the milling atmosphere

was subsequently modified to an inert Ar environment (FeCoNa-B25-4-Ar). The catalyst prepared under Ar exhibited a further increase in C_{5+} selectivity (~42.1%) and yield (~24.1%), while maintaining high CO_2 conversion (~57.3%) and comparable CH_4 selectivity. The product distribution included 23.0% selectivity to C_5-C_{10} hydrocarbons and 23.9% selectivity to C_8-C_{16} hydrocarbons, corresponding to gasoline- and jet-fuel-range fractions, respectively (**Table S3**). Combining the C_2-C_4 and C_{5+} hydrocarbon fractions with alcohol fractions, FeCoNa-B25-4-Ar reaches a total valuable product selectivity ($S(C_{2+})$) of 76.3%, corresponding to a yield of 43.7%. Relative to air milling, Ar milling increases the C_{5+} yield from 19.9% to 24.1%, at essentially unchanged CO_2 conversion. The improved catalytic performance of the Ar-milled catalyst can be attributed to the suppression of oxidation and enhanced preservation of metallic FeCo alloy and Fe-carbide phases during mechanochemical processing (**Fig. 2a** and **Table S1**). In contrast to air milling, Ar milling led to greater retention of carbide phase in the spent catalyst. We conclude that mechanochemical treatment under optimised inert conditions (25 Hz for 4 h) promotes the development of favourable surface-active phases for long-chain hydrocarbon formation during CO_2 hydrogenation.

The optimal FeCoNa-B25-4-Ar catalyst compares favourably with previous literature reports (**Table 1** and Supplementary Section S2.3) in terms of catalytic activity but is notably superior in long-term stability, which will be discussed in the following sections.

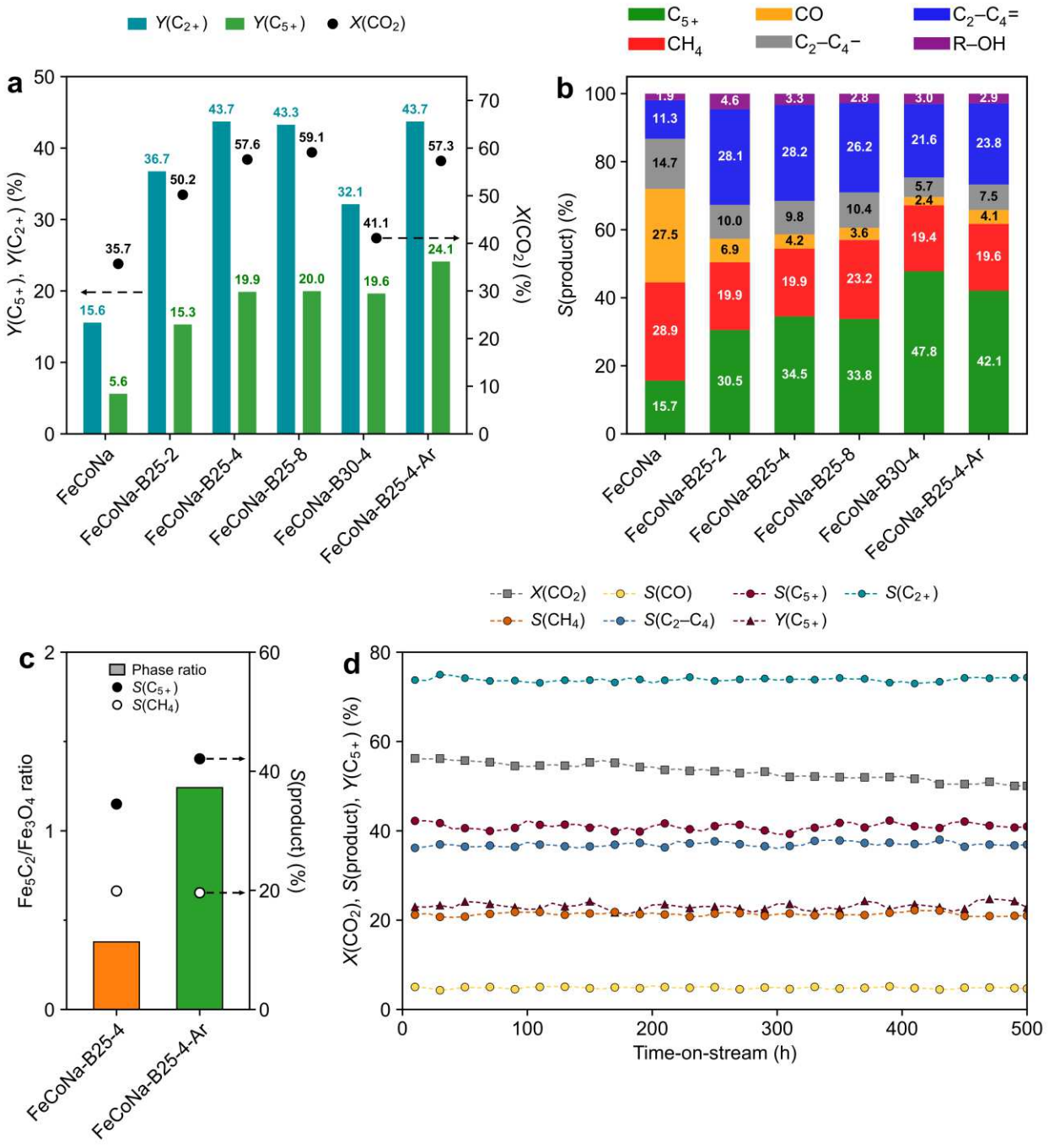


Fig. 3. **Catalytic performance of DJS-derived catalysts in CO_2 hydrogenation.** (a) CO_2 conversion, C_{2+} yield, C_{5+} yield and (b) product selectivity for catalysts prepared under different milling conditions. (c) C_{5+} and CH_4 selectivities as a function of the Fe_5C_2/Fe_3O_4 phase ratio for spent air- and Ar-milled catalysts. (d) Time-on-stream performance of FeCoNa-B25-4-Ar over 500 h. Reaction condition: 350 °C, 30 bar, $H_2/CO_2 = 3$, and GHSV = 5732 $cm^3\ h^{-1}\ g_{cat}^{-1}$.

Reaction-induced structural evolution of DJS-derived catalysts

To understand how the initially dense, low-surface-area DJS-derived pre-catalysts evolve into their catalytically active working state, N_2-sorption, XRD, and microscopy analyses were performed before and after CO_2 hydrogenation. N_2-sorption measurements (**Fig. S4-S5**) show an increase in BET surface areas from 1.3 and 0.7 $m^2\ g^{-1}$ in fresh samples to 5.1 and 5.2 $m^2\ g^{-1}$ after reaction, for FeCoNa-B25-4 and FeCoNa-B25-4-Ar, respectively (**Table S1**). This is in line with particle size distribution analysis (**Fig. S6**), where the mean particle size of fresh FeCoNa-B25-4-Ar is markedly reduced under CO_2 hydrogenation conditions, indicating substantial fragmentation. Such a phenomenon is particularly notable given the high density of the as-synthesised DJS materials, and contrasts with the surface-area loss associated with crystallite growth and water-induced sintering typically expected and reported for Fe- and other transition metal-based CO_2 hydrogenation catalysts synthesised by conventional methods.[11,29,37–39]

Comparing XRD patterns of fresh and spent catalysts (**Fig. 2b**), metallic Fe-based phases present in the fresh DJS materials prior to reaction are largely transformed upon reaction into Fe_3O_4 and Fe_5C_2, with mean crystallite sizes in the range of ~80-145 nm and ~36-45 nm, respectively, leaving a small FeCo fraction (~6 wt.%, **Table S1**) in the sample. This agrees with high-resolution Transmission Electron Microscopy (HR-TEM) imaging (**Fig. 4a-c**), which shows predominantly metallic FeCo planes in as-synthesised FeCoNa (**Fig. 4a**) which are retained following ball milling in Ar (**Fig. 4b**). Upon CO_2 hydrogenation (**Fig. 4c**), the spent FeCoNa-B25-4-Ar catalyst undergoes substantial phase evolution with the emergence of Fe_3O_4(311), Fe_5C_2(510), FeCo(110) and FeCo(200), confirming oxidation and carburisation of the initially metallic system with retention of alloy phase under CO_2 hydrogenation reaction conditions. Compared to fresh FeCoNa-B25-4-Ar, the spent catalyst also exhibits noticeable changes in morphology (**Fig. S7**). These

observations suggest that initial metallic FeCo-rich pre-catalyst restructures under CO_2 hydrogenation conditions, evolving towards a mixed oxide-carbide assemblage. Similar restructuring behaviour has been reported where metallic Fe phases undergo competitive oxidation and carburisation during CO_2 hydrogenation, leading to continuous structural evolution between Fe_3O_4 and Fe_5C_2 domains inducing lattice strain, defect formation, and surface roughening, which collectively promote fragmentation and the generation of new active oxide-carbide interfaces under reaction conditions.[11,40]

Notably, the formation of Fe_5C_2, widely associated with C-C coupling activity, is consistently observed in the spent catalysts, while oxide phases remain present, suggesting carburisation resulting in a dynamic equilibrium between oxidised and carburised states.[41] Ar milling preserved more Fe_5C_2 than air milling, yielding a spent catalyst with a higher carbide fraction (**Table S1**). The greater retention of catalytically active Fe_5C_2 could be associated with the higher activity of the Ar-milled catalyst, consistent with the reported activity loss upon carbide oxidation.[9] Residual FeCo detected in the spent catalyst may have played a crucial role as an intrinsic reduction promoter, helping to limit carbide re-oxidation.[42,43] While conventional precipitated Fe catalysts can undergo crystallite growth through sintering alongside carbide oxidation during Fischer-Tropsch synthesis,[44] DJS-derived catalysts experience phase transformation coupled with restructuring, where the development of oxide and carbide crystallites occurs alongside the generation of new surfaces and interfaces.

To further link the role of phase composition to catalytic performance, **Fig. 3c** compares the Fe_5C_2/Fe_3O_4 phase ratio of the spent air- and Ar-milled catalysts with their C_{5+} and CH_4 selectivities. At similar CO_2 conversions of 57.6% and 57.3%, the Ar-milled catalyst has a higher carbide-to-oxide ratio and higher C_{5+} selectivity (42.1% versus 34.5%), while CH_4 selectivity is

nearly unchanged. This suggests an association between a more carbide-rich working structure and higher C_{5+} selectivity, building on literature reports that coexisting carbide and oxide phases contribute differently to reactant adsorption and hydrocarbon formation.[7,45–47]

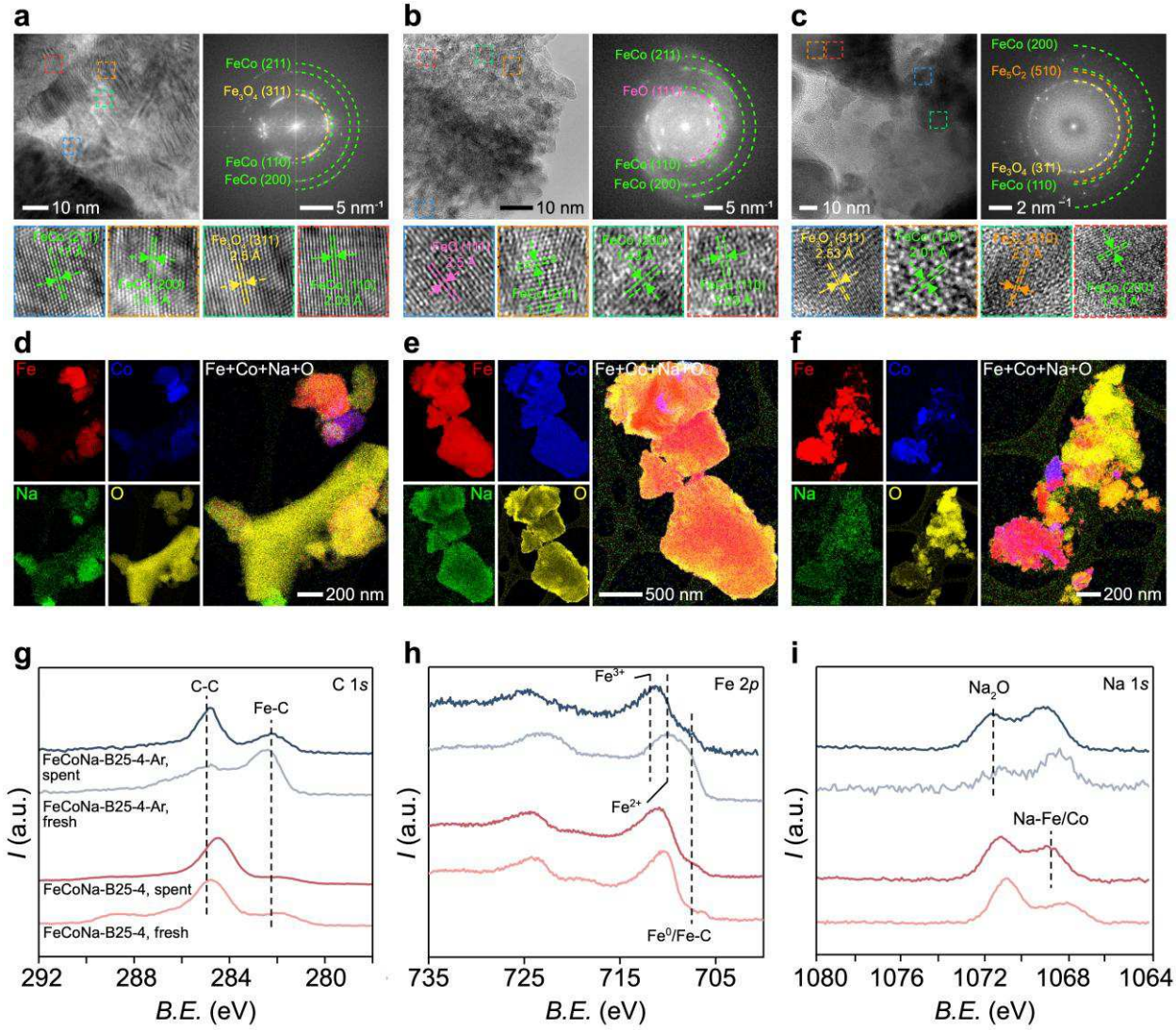


Fig. 4. **Microscopic and surface analysis of FeCoNa catalysts.** HR-TEM, Fast Fourier Transform (FFT) pattern, and lattice fringe analyses of (a) FeCoNa, (b) FeCoNa-B25-4-Ar, and (c) spent FeCoNa-B25-4-Ar catalysts. STEM-EDS and elemental mapping analyses of (d) FeCoNa, (e) FeCoNa-B25-4-Ar, and (f) spent FeCoNa-B25-4-Ar catalysts. X-ray Photoelectron Spectroscopy (XPS) core-level spectra of fresh and spent FeCoNa catalysts in the (g) C 1*s*, (h) Fe 2*p*, and (i) Na 1*s* regions.

Role and evolution of surface species

Scanning transmission electron microscopy coupled to energy-dispersive X-ray spectroscopy (STEM-EDS) and elemental mapping analyses indicate a homogeneous spatial distribution of Fe, Co, Na, and O throughout the surfaces of both fresh and spent catalysts (**Fig. 4d-f**). In the fresh FeCoNa and FeCoNa-B25-4-Ar samples, the Fe and Co signals strongly overlap, indicating the formation of mixed FeCo-rich domains. Sodium is also uniformly distributed across the particles, suggesting that the promoter remains well dispersed after DJS and post-high-energy ball milling. After the reaction, the spent FeCoNa-B25-4-Ar catalyst still exhibits overlapping Fe and Co distributions along with pronounced oxygen signals, consistent with the oxide-containing phases identified by HR-TEM (**Fig. 4a-c**) and XRD analyses (**Fig. 2b**). Additionally, the Na signal remains uniformly distributed throughout the spent catalyst, indicating that sodium stays associated with the catalyst surface during structural reconstruction rather than segregating into isolated domains.

To investigate the chemical state of surface species in as-synthesised and reacted catalysts, we conducted X-ray photoelectron spectroscopy (XPS) on selected samples. In the C 1*s* spectra (**Fig. 4g**), in addition to the adventitious carbon peak at 284.8 eV, a peak at ~282 eV can be observed in both fresh FeCoNa B25-4 and fresh FeCoNa B25-4-Ar, which can be assigned to carbon in metal carbide phases,[40] indicating that the DJS pre-catalyst is already carburised at the surface level. After the CO_2 hydrogenation, the peak intensity attributed to Fe-C surface species increases in the spent catalysts, consistent with further surface carburisation. This evolution is further supported by the Fe 2*p* spectra (**Fig. 4h**). For the fresh FeCoNa-B25-4, the Fe 2*p* region shows peaks at 710.2 and 711.1 eV, corresponding to Fe^{2+} and Fe^{3+} species, respectively. In addition, a distinct feature at ~706.7 eV in both fresh and spent catalysts can be assigned to metallic Fe,[41] but may also contain

Fe-C contributions.[11] Its persistence in the spent catalysts is consistent with the residual FeCo identified by XRD. These findings are in line with XRD results (**Fig. 2b**), suggesting that the DJS-derived FeCoNa-B25-4 catalyst possesses a partially oxidised surface while retaining a significant metallic character, rather than a wholly oxidic precursor surface as typically reported for Fe-based oxide precursors.[3] After CO_2 hydrogenation, a shoulder with lower binding energy (~707-708 eV) appears in the Fe $2p_{3/2}$ region for all spent samples, characteristic of iron carbide species, indicating that the catalyst surface evolves towards a more carbide-rich surface under CO_2 hydrogenation conditions while maintaining a fraction of oxidised species.

For the alkali promoter, the Na 1*s* spectra (**Fig. 4i**) shows an intense peak (~1071 eV) corresponding to Na_2O in all catalysts.[48] Crucially, we also observe another peak binding energy of ~1068 eV in the core-level scan of fresh FeCoNa-B25-4 and fresh FeCoNa-B25-4-Ar, which could be assigned to Na species in intimate electronic contact with metallic Fe-Co *via* O-bridged Na-O-Fe/Co interfacial sites.[49] Such species have been shown to enhance FT reaction by electronically enhancing CO back-donation and dissociation while disfavouring excessive hydrogen adsorption.[49] In the Co 2*p* spectra (**Fig. S8**), contributions from Co^{3+} and Co^{2+} are present, indicating that Co is primarily present in oxidic form as part of $(Fe_xCo_y)_3O_4$, but Co_2C-related features (~778 eV) could also be present after reaction.[50] These observations agree with STEM-EDS measurements (**Fig. 4, e-f**), which show that Na and Co are well-dispersed.

Long-term stability

The optimised FeCoNa-B25-4-Ar catalyst was tested for 500 h at 350 °C and 30 bar (**Fig. 3d**). CO_2 conversion remains stable in the range of 55% to 50% over 500 h time on stream, with C_{5+} selectivity in the range of 40-42%. The other major product selectivities were also essentially

stable over this period. The BET surface area of the recovered catalyst after 500 h was 16.5 m^2 g^{-1}, representing a 23.6x increase from the fresh sample (0.7 m^2 g^{-1}) and a continued increase from 24 h on stream (5.2 m^2 g^{-1}), indicating continued restructuring during prolonged reaction. Most notably, XRD of the catalyst recovered after 500 h (**Fig. S9**) identifies Fe_5C_2 and residual FeCo alongside Fe_3O_4. Thus, the alloy-rich precursor develops a carbide-containing working structure without undergoing complete oxidation during prolonged CO_2 hydrogenation. The role of this phase in preserving a reduced state is supported by thermogravimetric analysis (TGA, **Fig. S10**). Examining the percentage weight increase for the TGA measurement under air compared to under N_2 as a proxy indicator for phase oxidation, we observe that oxidation in fresh FeCoNa-B25-4-Ar generally occurs at higher temperatures than in its air-milled counterpart (**Fig. S10b**), hinting that the additional Fe_5C_2 present arising from argon milling provides greater resistance to oxidation upon heating. Similarly for the used catalysts, the significantly higher carbide proportion in FeCoNa-B25-4-Ar (52.0 wt.% Fe_5C_2 after 24 h *versus* 29.6 wt.% for air-milled FeCoNa-B25-4, **Table S1**) is also associated with a ~50°C increase in oxidation onset temperature (**Fig. S10d**). This suggests the role of FeCo retained during reaction as an intrinsic reduction promoter, favouring preservation of the carbide phases and improving resistance to re-oxidation.[42,43] Overall, these characteristics account for the unprecedented stability of FeCoNa-B25-4-Ar over 500 h, sustaining a consistent 50% CO_2 conversion without significant loss in activity or C_{5+} selectivity for a longer duration than previously reported catalysts (**Table 1** and Supplementary Section S2.3).

Mechanistic Insights of reactivity on the FeCo-Fe_5C_2-Fe_3O_4 surface

To rationalise the measured CO_2 hydrogenation activity, we computed the adsorption free energies (G_{ads}) of the key intermediates spanning the reaction network on χ-Fe_5C_2(510), Na_2O-promoted χ-Fe_5C_2(510), Fe_3O_4(111), and FeCo(110) (**Fig. 5**). Top-view geometries of all intermediates are

displayed in **Table S4**. This energetics assign each phase a distinct and complementary function. Fe_3O_4 activates CO_2, binds it strongly (G_{ads} = −1.96 eV and E_{ads} = −2.57 eV) in a bent, activated configuration, consistent with the geometry and adsorption energy (E_{ads} = −2.51 eV) previously reported for Fe_{oct2}-terminated Fe_3O_4 (111) surface.[51] Fe_3O_4 also stabilises the dissociation CO* product (G_{ads} = −2.02 eV) together with the first CO_2 hydrogenation intermediates (COOH*, −2.09 eV; HCOO*, −3.54 eV), thereby closing the rWGS branch of the tandem. The strong CO binding allows the oxide to act as a CO reservoir that feeds neighbouring carbide phase. χ-Fe_5C_2, by contrast, sits at the Sabatier optimum for CO binding (G_{ads} = −0.83 eV), binding it firmly enough to retain the CO flux supplied by the oxide yet weakly enough to permit scission to C*. Critically, the oxide destabilises atomic carbon (G_{ads} = +3.67 eV) while over-stabilising the terminal CH_x (CH_4*, −2.82 eV), making it a methane sink rather than a chain-growth surface. Unlike Fe_3O_4 , χ-Fe_5C_2 adsorbs the CH_x intermediates exergonically (C*, CH*, CH_2* at −0.06, −0.64, −0.42 eV, respectively). Since light olefins can re-enter the coupling sequence towards the formation C_{5+} products while saturated alkanes terminate it, the relative stabilities of C_2H_4 and C_2H_6 was used in this study to track the surface's hydrogenation tendency. χ-Fe_5C_2 was found to hold C_2H_4 far more loosely than Fe_3O_4 (G_{ads} = −0.59 eV vs -3.14 eV), identifying the carbide as the chain-growth phase.

FeCo supports the hydrogenation chemistry by supplying H* and CO* (H*, −0.34 eV; CO, −0.45 eV) and aiding the C_2 release through weak C_2H_4* binding (G_{ads} = −0.56 eV). The computed thermoneutral O* binding on FeCo (G_{ads} = −0.06 eV vs −1.00 eV on Fe_3O_4) reflects a weak driving force for re-oxidation, in line with previous studies showing that Co improves reducibility and limits carbide-to-oxide conversion.[43] Importantly, Na_2O tunes the carbide in three ways: (i) CO* binding strengthens by 0.20 eV, enriching the C* pool, consistent with previous theoretical

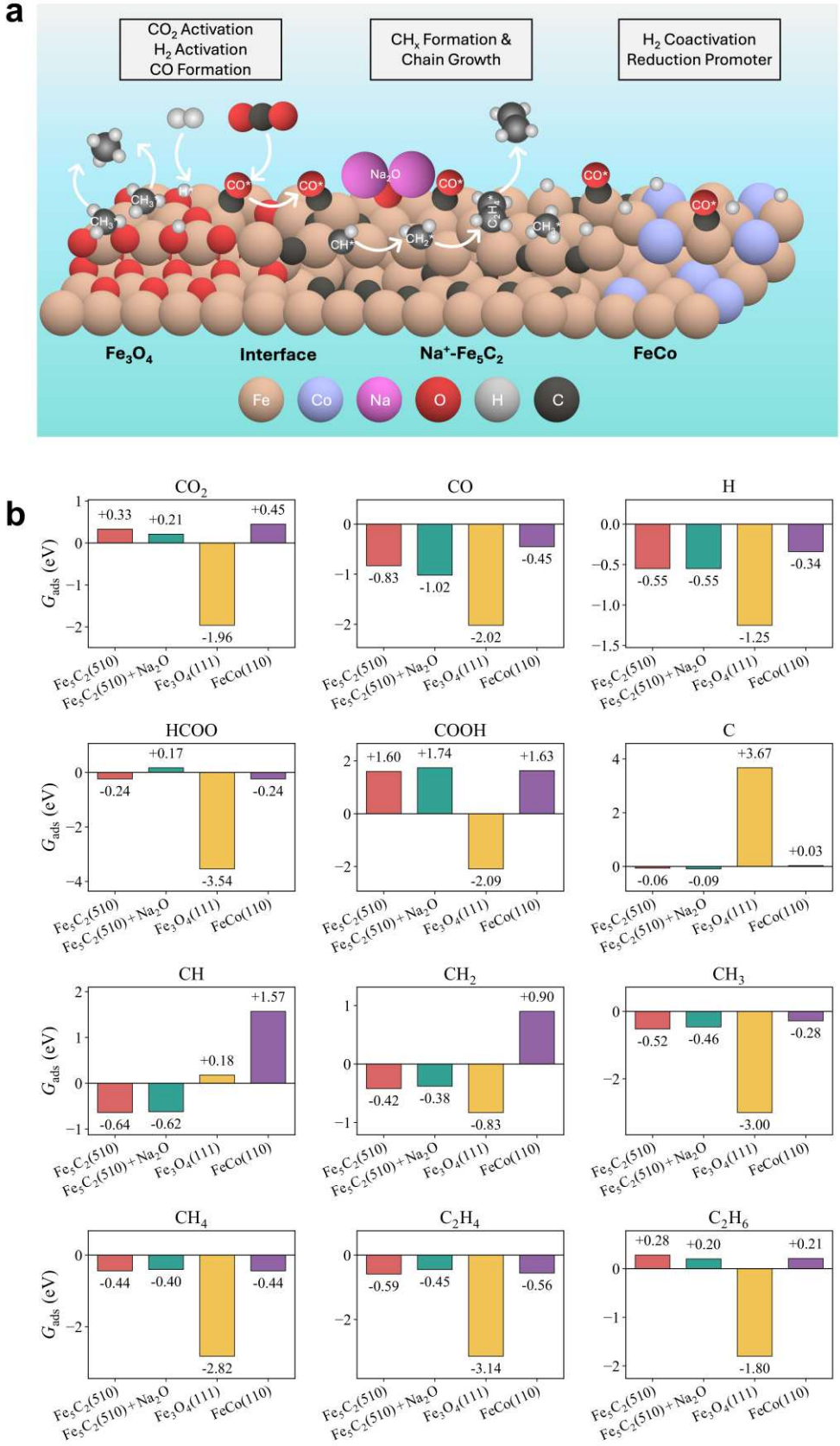

a
CO2 Activation
H2 Activation
CO Formation
CHx Formation &
Chain Growth
H2 Coactivation
Reduction Promoter
Na2O
CO*
CH3*
CH*
CH2*
CHx*
Fe3O4
Interface
Na+-Fe5C2
FeCo
Fe
Co
Na
O
H
C
b
CO2
CO
H
HCOO
COOH
C
CH
CH2
CH3
CH4
C2H4
C2H6
Gads (eV)
+0.33
+0.21
-1.96
+0.45
-0.83
-1.02
-2.02
-0.45
-0.55
-0.55
-1.25
-0.34
-0.24
+0.17
-3.54
-0.24
+1.60
+1.74
-2.09
+1.63
-0.06
-0.09
+3.67
+0.03
-0.64
-0.62
+0.18
+1.57
-0.42
-0.38
-0.83
+0.90
-0.52
-0.46
-3.00
-0.28
-0.44
-0.40
-2.82
-0.44
-0.59
-0.45
-3.14
-0.56
+0.28
+0.20
-1.80
+0.21
Fe5C2(510)
Fe5C2(510)+Na2O
Fe3O4(111)
FeCo(110)

Fig. 5. **Structural evolution and reaction mechanism of FeCoNa catalysts during CO_2 hydrogenation.** (a) Proposed reaction scheme informed by DFT adsorption calculations over the Fe_3O_4-Na-promoted Fe_5C_2-FeCo model surface, illustrating CO_2 activation and the subsequent formation of hydrocarbon products. (b) Gibbs free energies of adsorption (G_{ads}) of key reaction intermediates. Each panel corresponds to a single adsorbate species: CO_2, CO, H, COOH, HCOO, C, CH, CH_2, CH_3, and CH_4, and the C_2 products C_2H_4 and C_2H_6. Each species is adsorbed on the four catalyst surfaces: $Fe_5C_2(510)$, $Fe_5C_2(510)$ + Na_2O, $Fe_3O_4(111)$, and FeCo(110). More negative values indicate stronger (more favourable) adsorption, while positive values indicate endergonic, unfavourable binding. Values (in eV) are annotated above or below each bar.

results,[52] (ii) HCOO* destabilises by 0.41 eV, suppressing oxygenate routes, and (iii) $C_2H_4^*$ loosens, disfavouring secondary hydrogenation and preserving light olefins for further coupling, in agreement with previous studies.[53] The high olefin productivity is therefore not a property of any single iron phase but an emergent feature of an oxide/carbide tandem, mirroring the division of labour proposed for Na-Zn-Fe,[19] FeAlK,[54] and Na-Fe_3O_4/zeolite[37] catalysts, in which an oxide activates CO_2 while an alkali-promoted carbide forms and releases the olefin.

CONCLUSIONS

Direct Joule Synthesis followed by high-energy milling provides a rapid, solvent-free route to FeCoNa catalysts with high CO_2 hydrogenation activity and sustained C_{2+} and C_{5+} selectivity. Using FeCoNa as a representative composition, optimisation of DJS and ball milling procedures revealed milling at 25 Hz for 4h under argon to produce materials with the highest catalytic activity. The optimised FeCoNa-B25-4-Ar catalyst achieves 57.3% CO_2 conversion, selectivities of 76.3% and 42.1% to total C_{2+} and C_{5+} products respectively, and C_{2+} and C_{5+} yields of 43.7% and 24.1% respectively, at 350 °C, 30 bar and GHSV = 5732 $cm^3\ h^{-1}\ g_{cat}^{-1}$. At a higher space

velocity of 11464 cm^3 h^{-1} g_{cat}^{-1}, a C_{2+} and C_{5+} space-time yield of 0.68 $g_{C_{2+}}$ h^{-1} g_{cat}^{-1} and 0.4 $g_{C_{5+}}$ h^{-1} g_{cat}^{-1} was attained, exceeding the productivity reported by literature benchmarks. During a long-term stability test, C_{2+} and C_{5+} selectivity remains approximately 76-78% and 40-42% respectively with minimal drop in CO_2 conversion for at least 500 h on stream, again exceeding other reports in the literature. Physical characterisation and electron microscopy reveal that the as-milled FeCo-rich, low-surface area precursor reconstructs into an Fe_3O_4-Fe_5C_2-containing material with detectable residual FeCo after prolonged operation. The persistence of FeCo as a reduction promoter provides resistance to excessive re-oxidation, contributing to the superior stability of FeCoNa-B25-4-Ar, in addition to further mechanistic roles in supplying adsorbed H* and CO* as well as aiding olefin release as determined by DFT calculations. In contrast to employing Fe oxide-based starting materials synthesised by conventional methods, this work advances the use of a metallic phase-rich precursor whose reaction-induced reconstruction generates and maintains a productive multiphase catalyst active structure. These findings affirm that catalytic performance is governed by dynamic restructuring under reaction conditions, and establish DJS as a promising rapid, solvent-free route for generating highly adaptable catalyst materials for CO_2 hydrogenation.

METHODS

Catalyst Synthesis

Direct Joule Synthesis (DJS) strategy was used to synthesise Fe-based catalysts (**Fig. 1a**).[17] For a resultant composition of $Fe_{85}Co_{10}Na_5$, powders of Fe (Sigma Aldrich, ≥99%, reduced, powder (fine)), Co (Sigma Aldrich, <150 μm, 99.9% trace metals basis), and $NaNO_3$ (Sigma Aldrich, ≥99.0%) in the molar ratio of Fe:Co:Na = 85:10:5 were homogeneously mixed using a planetary

ball mill (QM04, CHISHUN Tech) at 600 rpm for a total duration of 150 minutes, divided into 5 cycles of alternating 15 min clockwise and 15 min anticlockwise rotations. The resulting powder mixture was subsequently dried in a vacuum oven at 50 °C for 2 h. The dried powder was then sandwiched between several carbon felt discs (16 mm diameter) placed inside a quartz tube. A graphite rod (16 mm diameter) was used to establish electrical contact between the carbon felt and conductive copper tape. A DC power supply (eTOMMENS-6020C) was employed to supply current and voltage in the ranges of 0-20 A and 0-60 V, respectively. During the synthesis process, the internal temperature of the quartz tube was monitored using an infrared (IR) thermometer (YCR, D30180AR). The obtained powder was denoted as FeCoNa. Subsequently, the DJS-synthesised powder was further subjected to ball milling using a Retsch Mixer Mill MM500 at 25-30 Hz for 2-8 h under an air atmosphere, employing two stainless steel balls with a diameter of 1.5 cm. The resulting ball-milled sample was denoted as FeCoNa-Bx-y, where B, x, and y stand for Ball milling, the frequency (in Hertz), and time (in hours), respectively. In addition, ball milling was also carried out for FeCoNa at 25 Hz for 4 h under an Ar atmosphere, and the resulting sample was denoted as FeCoNa-B25-4-Ar.

Catalyst characterisation

Catalyst samples collected at different stages of synthesis, activation, and reaction, including samples recovered after different times on stream, were characterised using X-ray diffraction (XRD), N_2 physisorption, scanning electron microscopy coupled with energy-dispersive X-ray spectroscopy (SEM-EDS), high-resolution transmission electron microscopy and selected-area electron diffraction (HR-TEM/SAED), scanning transmission electron microscopy coupled with EDS elemental mapping (STEM-EDS), X-ray photoelectron spectroscopy (XPS), and

Thermogravimetric Analysis (TGA). Detailed experimental conditions, sample-preparation procedures, and data-analysis methods are provided in the Supporting Information (Section S1.1).

Catalyst testing

CO_2 hydrogenation was evaluated in a 16-channel continuous-flow fixed-bed reactor system.[55] Catalysts were reduced in H_2 at 400 °C, activated in H_2/CO at 300 °C and 10 bar, and subsequently tested at 350 °C and 30 bar using a 3:1 H_2/CO_2 feed at a standard GHSV of 5732 $cm^3\ h^{-1}\ g_{cat}^{-1}$. An additional productivity test used a GHSV of 11464 $cm^3\ h^{-1}\ g_{cat}^{-1}$ at 350 °C and 30 bar. Product distributions were quantified by online gas chromatography using Ar as an internal standard. Detailed reactor specifications, pretreatment procedures, product quantification, and calculation methods are provided in the Supporting Information (Section S1.2).

Computational Methods

Spin-polarised DFT calculations were performed using the Vienna Ab-initio Simulation Package (VASP).[56–58] Exchange-correlation effects were treated within the generalised gradient approximation using the functional of Perdew, Burke, and Ernzerhof,[59] and the core-valence electron interaction was described by the projector augmented wave method.[60,61] The solution of the Kohn-Sham equations was expanded in a plane wave basis set with a cutoff energy of 520 eV, and the sampling of the Brillouin zone was performed using a Monkhorst-Pack scheme.[62] Geometry optimisations were carried out using the conjugate gradient method and converged to a threshold of 10^{-6} eV. The structures were relaxed until the force on each atom in every Cartesian direction fell below 0.01 eV/Å. Electron smearing was employed *via* the Methfessel-Paxton technique with a smearing width of 0.2 eV.[63] Van der Waals interactions were accounted for using

Grimme's D3 dispersion correction method.[64] The modelling of structures used in DFT calculations is detailed in the Supporting Information (Section S1.3).

REFERENCES

1. Loh, J. Y. Y., Kherani, N. P. & Ozin, G. A. Persistent CO_2 photocatalysis for solar fuels in the dark. *Nat. Sustain.* **4,** 466–473 (2021).
2. Gao, P. *et al.* Direct conversion of CO_2 into liquid fuels with high selectivity over a bifunctional catalyst. *Nat. Chem.* **9,** 1019–1024 (2017).
3. Yao, B. *et al.* Transforming carbon dioxide into jet fuel using an organic combustion-synthesized Fe-Mn-K catalyst. *Nat. Commun.* **11,** 6395 (2020).
4. Santos, J. L. *et al.* Bayesian optimization guides the discovery of high-performance catalysts for direct CO_2-to-jet-fuel conversion. *Chem Catal.* **6,** 101683 (2026) doi:10.1016/j.checat.2026.101683.
5. Zhang, L. *et al.* Long-Term CO_2 Hydrogenation into Liquid Fuels with a Record-High Single-Pass Yield of 31.7% over Interfacial Fe–Zn Sites. *Nano Lett.* **25,** 4904–4912 (2025).
6. Nielsen, M. R. *et al.* Reduction and carburization of iron oxides for Fischer–Tropsch synthesis. *J. Energy Chem.* **51,** 48–61 (2020).
7. Yang, Q. & Kondratenko, E. V. From Understanding of Catalyst Functioning toward Controlling Selectivity in CO_2 Hydrogenation to Higher Hydrocarbons over Fe-Based Catalysts. *Acc. Mater. Res.* **5,** 1314–1328 (2024).
8. Guo, L. *et al.* High-yield production of liquid fuels in CO_2 hydrogenation on a zeolite-free Fe-based catalyst. *Chem. Sci.* **14,** 171–178 (2023).

9. Claeys, M. *et al.* Oxidation of Hägg Carbide during High-Temperature Fischer–Tropsch Synthesis: Size-Dependent Thermodynamics and In Situ Observations. *ACS Catal.* **11,** 13866–13879 (2021).

10. Ye, R.-P. *et al.* CO_2 hydrogenation to high-value products via heterogeneous catalysis. *Nat. Commun.* **10,** 5698 (2019).

11. Zhu, J. *et al.* Dynamic structural evolution of iron catalysts involving competitive oxidation and carburization during CO_2 hydrogenation. *Sci. Adv.* **8,** eabm3629 (2022).

12. Qian, F. *et al.* Stabilized Fe_7C_3 catalyst with K–Mg dual promotion for robust CO_2 hydrogenation to high-value olefins. *Nat. Commun.* **16,** 8044 (2025).

13. Amrute, A. P., de Bellis, J., Felderhoff, M. & Schüth, F. Mechanochemical Synthesis of Catalytic Materials. *Chem. Eur. J.* **27,** 6819–6847 (2021).

14. Amrute, A. P., Łodziana, Z., Schreyer, H., Weidenthaler, C. & Schüth, F. High-surface-area corundum by mechanochemically induced phase transformation of boehmite. *Science* **366,** 485–489 (2019).

15. Dong, H. *et al.* Flash Joule Heating: A Promising Method for Preparing Heterostructure Catalysts to Inhibit Polysulfide Shuttling in Li-S Batteries. *Adv. Sci.* **11,** e2405351 (2024).

16. Liu, Y. *et al.* Ultrafast Joule heating technology for functional nanomaterials synthesis: Recent progress, challenges, and perspectives. *Mater. Rep. Energy* **5,** 100377 (2025).

17. Zhang, C. *et al.* Direct Joule-Heated Non-Equilibrium Synthesis Enables High Performing Thermoelectrics. Preprint at https://doi.org/10.48550/arXiv.2506.04447 (2025).

18. Liang, B. *et al.* Effect of Na Promoter on Fe-Based Catalyst for CO_2 Hydrogenation to Alkenes. *ACS Sustain. Chem. Eng.* **7,** 925–932 (2019).

19. Zhang, Z. *et al.* Selective hydrogenation of CO_2 and CO into olefins over Sodium- and Zinc-Promoted iron carbide catalysts. *J. Catal.* **395,** 350–361 (2021).

20. Behvandi, A., Shokrollahi, H., Chitsazan, B. & Ghaffari, M. Magnetic and structural studies of mechanically alloyed nanostructured $Fe_{49}Co_{49}V_2$ powders. *J. Magn. Magn. Mater.* **322,** 3932–3937 (2010).

21. Gheisari, Kh., Javadpour, S., Oh, J. T. & Ghaffari, M. The effect of milling speed on the structural properties of mechanically alloyed Fe–45%Ni powders. *J. Alloys Compd.* **472,** 416–420 (2009).

22. Park, S. W. *et al.* High-Throughput Synthesis of Mn-Based Disordered Rock-Salt Li-Ion Cathodes with Improved Rate Capability via Rapid Joule-Heating. *Adv. Energy Mater.* **15,** e03496 (2025).

23. Wang, X. *et al.* Synthesis of isoalkanes over a core (Fe–Zn–Zr)–shell (zeolite) catalyst by CO_2 hydrogenation. *Chem. Commun.* **52,** 7352–7355 (2016).

24. Shi, Z. *et al.* Effect of alkali metals on the performance of $CoCu/TiO_2$ catalysts for CO_2 hydrogenation to long-chain hydrocarbons. *Chin. J. Catal.* **39,** 1294–1302 (2018).

25. Choi, Y. H. *et al.* Carbon dioxide Fischer-Tropsch synthesis: A new path to carbon-neutral fuels. *Appl. Catal. B: Environ.* **202,** 605–610 (2017).

26. Boreriboon, N., Jiang, X., Song, C. & Prasassarakich, P. Fe-based bimetallic catalysts supported on TiO_2 for selective CO_2 hydrogenation to hydrocarbons. *J. CO_2 Util.* **25,** 330–337 (2018).

27. Albrecht, M. *et al.* Unexpectedly efficient CO_2 hydrogenation to higher hydrocarbons over non-doped Fe_2O_3. *Appl. Catal. B: Environ.* **204,** 119–126 (2017).

28. Choi, Y. H. *et al.* Sodium-Containing Spinel Zinc Ferrite as a Catalyst Precursor for the Selective Synthesis of Liquid Hydrocarbon Fuels. *ChemSusChem* **10,** 4764–4770 (2017).

29. Numpilai, T. *et al.* Structure–activity relationships of Fe-Co/K-Al_2O_3 catalysts calcined at different temperatures for CO_2 hydrogenation to light olefins. *Appl. Catal. A: Gen.* **547,** 219–229 (2017).

30. Guo, L. *et al.* Boosting liquid hydrocarbons selectivity from CO_2 hydrogenation by facilely tailoring surface acid properties of zeolite via a modified Fischer-Tropsch synthesis. *Fuel* **306,** 121684 (2021).

31. Jiang, F., Liu, B., Geng, S., Xu, Y. & Liu, X. Hydrogenation of CO_2 into hydrocarbons: enhanced catalytic activity over Fe-based Fischer–Tropsch catalysts. *Catal. Sci. Technol.* **8,** 4097–4107 (2018).

32. Noreen, A. *et al.* One-pass Hydrogenation of CO_2 to Multibranched Isoparaffins over Bifunctional zeolite-based Catalysts. *ACS Catal.* **10,** 14186–14194 (2020).

33. Wei, J. *et al.* New insights into the effect of sodium on Fe_3O_4-based nanocatalysts for CO_2 hydrogenation to light olefins. *Catal. Sci. Technol.* **6,** 4786–4793 (2016).

34. Zhang, Z. *et al.* Zn and Na promoted Fe catalysts for sustainable production of high-valued olefins by CO_2 hydrogenation. *Fuel* **309,** 122105 (2022).

35. Zhang, L. *et al.* Direct conversion of CO_2 to a jet fuel over CoFe alloy catalysts. *The Innovation* **2,** 100170 (2021).

36. Pan, M. *et al.* Unraveling the role of reaction intermediates in CO_2 hydrogenation to light aromatics over iron-based multifunctional catalysts. *Appl. Catal. B: Environ. Energy* **398,** 127033 (2026).

37. Wei, J. *et al.* Directly converting CO_2 into a gasoline fuel. *Nat. Commun.* **8,** 15174 (2017).

38. Ge, Y. *et al.* Descriptors toward higher alcohols and olefins formation in CO_2 hydrogenation on promoted iron catalysts. *Appl. Catal. B: Environ. Energy* **378,** 125578 (2025).

39. Hansen, T. W., DeLaRiva, A. T., Challa, S. R. & Datye, A. K. Sintering of catalytic nanoparticles: particle migration or Ostwald ripening? *Acc. Chem. Res.* **46,** 1720–1730 (2013).

40. Ge, Y. *et al.* Defective zirconia promotes monometallic iron catalysts for higher alcohol synthesis. *Chem Catal.* **4,** 101010 (2024).

41. Krausser, L. *et al.* Formation and Role of Iron-Containing Phases in CO_2 Hydrogenation to Higher Hydrocarbons. *ACS Catal.* **15,** 10627–10638 (2025).

42. Wang, W. *et al.* Bimetallic Fe–Co catalysts for the one step selective hydrogenation of CO_2 to liquid hydrocarbons. *Catal. Sci. Technol.* **13,** 1527–1540 (2023).

43. Dolsiririttigul, N. *et al.* Exploring the impact of cobalt and H_2 to CO ratios on catalytic performance of FeKAl and FeCoKAl catalysts in CO hydrogenation to light olefins. *Fuel* **383,** 133833 (2025).

44. Li, H. *et al.* Effect of reaction temperature and H_2/CO ratio on deactivation behavior of precipitated iron Fischer-Tropsch synthesis catalyst. *Catal. Today* **405–406,** 277–284 (2022).

45. Zhu, J., Shaikhutdinov, S. & Cuenya, B. R. Structure–reactivity relationships in CO_2 hydrogenation to C_{2+} chemicals on Fe-based catalysts. *Chem. Sci.* **16,** 1071–1092 (2025).

46. Najari, S. *et al.* Synergistic enhancement of CO_2 hydrogenation to C_{5+} hydrocarbons using mixed Fe_5C_2 and Na-Fe_3O_4 catalysts: Effects of oxide/carbide ratio, proximity, and reduction. *Chem. Eng. J.* **485,** 149787 (2024).

47. Chen, B. *et al.* Oxygen-driven restructuring of Fe_5C_2 inhibits the Iron-based catalyst C-C coupling in CO_2 hydrogenation. *Chem. Eng. J.* **538,** 176752 (2026).

48. Schmidt, C. & Kureti, S. CO_2 Conversion by Fischer-Tropsch Synthesis Using Na-Modified Fe Catalysts. *Chem. Ing. Tech.* **94,** 1747–1755 (2022).

49. Németh, M. *et al.* Na-promoted Ni/ZrO_2 dry reforming catalyst with high efficiency: details of Na_2O-ZrO_2-Ni interaction controlling activity and coke formation. *Catal. Sci. Technol.* **7,** 5386–5401 (2017).

50. Wang, M. *et al.* Stabilizing Co_2C with H_2O and K promoter for CO_2 hydrogenation to C_{2+} hydrocarbons. *Sci. Adv.* **9,** eadg0167 (2023).

51. Nie, X. *et al.* DFT insight into the effect of potassium on the adsorption, activation and dissociation of CO_2 over Fe-based catalysts. *Phys. Chem. Chem. Phys.* **20,** 14694–14707 (2018).

52. Ren, X., Men, Z., Wang, P., Filot, I. A. W. & Hensen, E. J. M. The nature of K promotion of χ-Fe_5C_2 for high chain-growth probability in the Fischer–Tropsch reaction. *Appl. Catal. B: Environ. Energy* **374,** 125403 (2025).

53. Liu, X. *et al.* Revealing the Effect of Sodium on Iron-Based Catalysts for CO_2 Hydrogenation: Insights from Calculation and Experiment. *J. Phys. Chem. C* **125,** 7637–7646 (2021).

54. Zhang, J. *et al.* Synergistic Surface and Bulk Engineering Enables Optimal χ-Fe_5C_2/Fe_3O_4 Interfaces on FeAlK Catalysts for Efficient CO_2 Hydrogenation to Heavy Olefins. *ACS Catal.* **16,** 8368–8385 (2026).

55. Zou, T., Zhang, J., Chen, B. W. J., Lim, Y.-F., Verma, S., Srinivasappa, P. M., Ng, C. Q. J., Gwie, C. G., Chen, L., Sato, K., Sullivan, M. B., Borgna, A., Hippalgaonkar, K. & Amrute, A. Integrating AI with automated high-throughput methods for the discovery of novel catalysts. *ACS Catalysis*, *under review* (2026).

56. Kresse, G. & Furthmüller, J. Efficiency of ab-initio total energy calculations for metals and semiconductors using a plane-wave basis set. *Comput. Mater. Sci.* **6,** 15–50 (1996).

57. Kresse, G. & Hafner, J. Ab initio molecular dynamics for liquid metals. *Phys. Rev. B* **47,** 558–561 (1993).

58. Kresse, G. & Hafner, J. Ab initio molecular-dynamics simulation of the liquid-metal-amorphous-semiconductor transition in germanium. *Phys. Rev. B* **49,** 14251–14269 (1994).

59. Perdew, J. P., Burke, K. & Ernzerhof, M. Generalized Gradient Approximation Made Simple. *Phys. Rev. Lett.* **77,** 3865–3868 (1996).

60. Kresse, G. & Joubert, D. From ultrasoft pseudopotentials to the projector augmented-wave method. *Phys. Rev. B* **59,** 1758–1775 (1999).

61. Blöchl, P. E. Projector augmented-wave method. *Phys. Rev. B* **50,** 17953–17979 (1994).

62. Monkhorst, H. J. & Pack, J. D. Special points for Brillouin-zone integrations. *Phys. Rev. B* **13,** 5188–5192 (1976).

63. Methfessel, M. & Paxton, A. T. High-precision sampling for Brillouin-zone integration in metals. *Phys. Rev. B* **40,** 3616–3621 (1989).

64. Grimme, S., Antony, J., Ehrlich, S. & Krieg, H. A consistent and accurate ab initio parametrization of density functional dispersion correction (DFT-D) for the 94 elements H-Pu. *J. Chem. Phys.* **132,** 154104 (2010).

ACKNOWLEDGEMENTS

A.A. and K.H. acknowledge funding support from NRF's CREATE Thematic Programme for Decarbonisation. A.A. acknowledges equipment time from A*STAR's Accelerated Catalyst Development Platform (IAF-PP: A19E9a0103) and A*STAR's Career Development Fund grant

(C210812023). Facility for Analysis, Characterisation, Testing and Simulation (FACTS) at Nanyang Technological University (NTU), Singapore, is acknowledged for use of its electron microscopy/X-ray facilities. J.R.-G. thanks Dr. Haiwen Dai for assistance in conducting XPS measurements. Apoorva Ravi is thanked for performing TGA measurements. M.A. acknowledges funding support from the Bakar Institute of Digital Materials for the Planet Postdoctoral Fellowship. The research was performed using computational resources sponsored by the Department of Energy's Office of Critical Minerals and Energy Innovation and located at the National Laboratory of the Rockies.

FUNDING

AxCIS Lab project under NRF's CREATE Thematic Programme for Decarbonisation ($ISCE^2$ grant number: SC22/24-7370EA). Agency for Science, Technology and Research (A*STAR)'s Industry Alignment Fund – Pre-Positioning grant (IAF-PP grant number: A19E9a0103). A*STAR's Career Development Fund grant (C210812023).

AUTHOR CONTRIBUTIONS

A.A. and K.H. conceptualised the research plan, supervised all stages of the research, and prepared the structure of the manuscript. J.R.-G. tuned the DJS method for catalyst synthesis. S.V., S.L., and D.T. performed DJS catalyst synthesis and carried out single-reactor and high-throughput reactor catalytic testing. P.M.S. and T.Z. assisted in catalytic testing and characterisation. M.A. performed DFT work under the supervision of K.A.P. P.Y.M. carried out post-milling and assisted with catalytic reactions. C.Q.J.N. and C.G.G. performed high-throughput catalytic experiments. J.R.-G. performed X-ray photoelectron spectroscopy. C.Z. and Z.A. performed transmission electron microscopy. Other characterisations were performed by J.R.-G., S.V., S.L., D.T., and

P.Y.M. S.V., J.R.-G., M.A., and T.Z. drafted the original manuscript. A.A., K.H., and K.A.P. corrected the manuscript. All authors revised the manuscript and gave approval to final version.

COMPETING INTERESTS

Authors declare no competing interests.

DATA CODE AND MATERIALS AVAILABILITY

All data and materials are available in the MS and SI.

Supplementary Files

This is a list of supplementary files associated with this preprint. Click to download.

- NatCommunSI.pdf